Infrared complex refractive indices of supercooled liquid HNO₃/H₂O aerosols

M. L. Norman, J. Qian, and R. E. Miller

Department of Chemistry, University of North Carolina, Chapel Hill

D. R. Worsnop

Center for Aerosol and Cloud Chemistry, Aerodyne Research, Inc., Billerica, Massachusetts

Abstract. Complex refractive indices have been retrieved for the first time directly from the Fourier transform infrared extinction spectra of supercooled liquid HNO_3/H_2O aerosols at 220 K. Aerosol compositions were determined by simultaneously monitoring equilibrium HNO_3 and H_2O vapor pressures with a tunable diode laser. The new optical constants are compared with previous results from room temperature bulk solutions and < 160 K amorphous solid thin films, and the differences are explained primarily in terms of the temperature-dependent dissociation of molecular HNO_3 into its constituent ions. Mie scattering analysis of aerosol extinction spectra suggests that using either the room temperature liquid or the amorphous solid refractive indices may result in inaccurate particle size determination. These new data sets are directly applicable to the characterization of polar stratospheric clouds through spectroscopic remote sensing.

1. Introduction

Polar stratospheric clouds (PSCs) play a well-established role in the heterogeneous chemical processing that leads to Antarctic ozone depletion [*Molina*, 1991; *Toon and Turco*, 1991]. Nevertheless, the aerosols contained in these clouds are still not well characterized. Although Type II PSCs are known to consist primarily of water ice particles formed below the frost point, the exact phase and composition of Type I PSCs are not known [*Molina*, 1991]. From early laboratory vapor pressure measurements it was concluded that Type I PSCs formed during the polar winter were likely composed of the most stable phase of solid nitric acid, crystalline nitric acid trihydrate (NAT) [*Hanson and Mauersberger*, 1988a], or perhaps metastable nitric acid dihydrate (NAD) [*Worsnop et al.*, 1993]. More recently, it has been proposed that PSC aerosols are composed of supercooled liquid nitric acid or a ternary solution with H_2O and H_2SO_4 [*Carslaw et al.*, 1994; *Drdla et al.*, 1994; *Arnold*, 1992]. In fact, analysis of Arctic field measurements indicates that liquid aerosols typically do not freeze before ice formation [*Waibel et al.*, 1999]. The uncertainty of this issue has prompted major research efforts toward Type I PSC characterization within the last decade, with an ever increasing focus on supercooled liquid properties.

Airborne remote sensing experiments have produced infrared spectra of PSC aerosols [*Kinne et al.*, 1989] as they exist in the stratosphere, while laboratory spectroscopic studies of aerosols [*Disselkamp et al.*, 1996; *Bertram and Sloan*, 1998] have also been carried out under near-stratospheric conditions. In both cases, Mie scattering theory

is typically used to model aerosol size, number density, and composition. This requires that the frequency-dependent optical constants be known for the aerosol systems in question. Although these complex refractive indices are available for room temperature binary HNO_3/H_2O solutions [*Querry and Tyler*, 1980; *Boone et al.*, 1980; *Remsberg et al.*, 1974] and for colder temperature crystalline [*Toon et al.*, 1994; *Niedziela et al.*, 1998a; *Richwine et al.*, 1995] and amorphous [*Toon et al.*, 1994] solid mixtures, no such data currently exist for supercooled liquid solutions. One reason for this is simply related to the experimental difficulties associated with producing supercooled bulk solutions or thin films under well-defined, low-temperature conditions. Often, the optical constants of amorphous nitric acid solids at much lower temperatures are assumed to be the same as those of supercooled solutions at stratospheric temperatures, given that their infrared absorption spectra are similar [*Toon et al.*, 1994]. This assumption seems reasonable given that HNO_3 is a strong acid that is usually considered to be fully dissociated at all concentrations. If this is strictly the case, we would not expect to see the kind of temperature-dependent ionic equilibrium changes that are observed in some other systems, including diprotic H_2SO_4 [*Niedziela et al.*, 1998b]. Nonetheless, a recent aerosol study by *Disselkamp et al.* [1996] showed that amorphous solid optical constants resulted in poor fits to supercooled liquid aerosol spectra in Mie scattering calculations, suggesting that the above assumption may be invalid.

We report here the first measurements of the frequency-dependent infrared optical constants of supercooled binary HNO_3/H_2O solutions. Our new data sets have been determined from 755 to 4700 cm⁻¹ by fitting the Fourier transform extinction spectra of laboratory-generated aerosols studied in a laminar flow cell at 220 K. Five solution compositions ranging from 35 to 70 wt % HNO_3 were accurately determined by simultaneous in situ monitoring of water and nitric acid vapor pressures using tunable diode laser
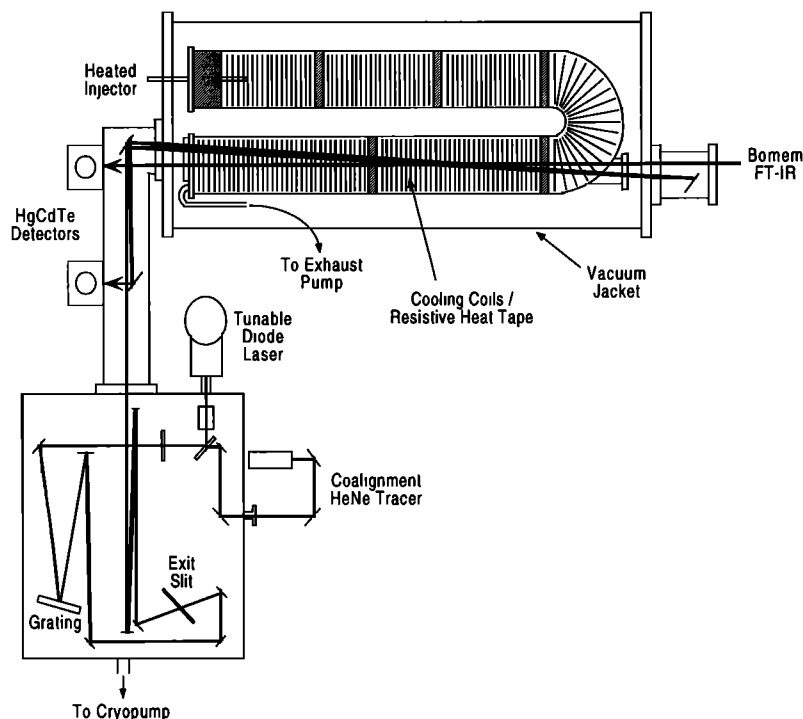
Figure 1. Schematic diagram of the aerosol flow cell, coupled with the Fourier Transform Infrared (FTIR) and tunable diode laser (TDL) systems.

spectroscopy. Our results show that there are significant differences between the supercooled liquid, the room temperature liquid [*Querry and Tyler*, 1980], and the amorphous solid thin film [*Toon et al.*, 1994] data. Only the new optical constants accurately reproduce supercooled nitric acid aerosol spectra using Mie scattering theory. We attribute the differences primarily to the fact that HNO₃ is not fully dissociated in this concentration range and that cooling the solution promotes dissociation into nitrate and hydronium ions, which in turn changes the associated absorption bands. These new data sets should significantly improve the accuracy of spectroscopic remote sensing data analyses in which supercooled liquid nitric acid solutions are considered.

2. Experimental Method

2.1. Aerosol Generation and Infrared Spectroscopy

In the present experiments, supercooled liquid HNO₃/H₂O aerosols were generated and analyzed using a laminar flow cell apparatus described in detail elsewhere [*Niedziela et al.*, 1999]. The cell, shown in Figure 1, is a 7.62 cm diameter gold-plated copper tube consisting of six sections. The temperature of each section is controlled independently to within ±1 K by balancing chilled N₂ gas flow with resistive heating. The cell geometry allows separate control of the aerosol formation and observation temperatures, while affording a 116 cm single-pass optical path length. Liquid aerosols were formed using two different methods, depending on the desired particle sizes. Small particles (0.2 - 0.5 μm radius) were formed by flowing helium buffer gas over a pool of room temperature, 71 wt % HNO₃ at rates of 200 - 1300 standard cubic centimeters per minute (sccm), and injecting

the equilibrium acid vapor into the top of the cell. The first two sections of the flow cell were held at 175 - 220 K, causing the injected vapor to become supersaturated with respect to HNO₃ and causing droplets to form by homogeneous nucleation and condensation [*McDonald*, 1962]. The smallest liquid particles were made at the lowest temperature (175 K). At even lower temperatures, water ice was formed, particularly in the more dilute aerosols, as indicated by the appearance of a sharp ice absorption feature at 3300 cm⁻¹. Larger particles (≥ 0.5 μm radius) were made by flowing the helium buffer through a glass frit immersed in the room temperature liquid HNO₃. The aerosols that formed by mechanical dispersion of the liquid [*Ulevicius et al.*, 1997] were injected into the top portion of the flow cell, and all sections were maintained at 220 K. For both of these generation methods the aerosol composition was varied by metering a flow of chromatography-grade water vapor into the nitric acid aerosol stream. The humidified stream was diluted with additional helium buffer gas, and the total flow rate was adjusted to maintain a steady state total cell pressure between 80 and 120 torr. Fourier transform infrared (FTIR) extinction spectra were recorded through the bottom sections of the cell using a Bomem DA3.02 spectrometer and HgCdTe detector. These spectra cover the midinfrared range from 755 to 4700 cm⁻¹, limited primarily by the ZnS (Cleartran) window cutoff at long wavelengths. Each spectrum represents the coaddition of 50 scans at 2 cm⁻¹ resolution. At the flow rates noted above, the residence time for a given aerosol was approximately 5 min. Spectra were therefore collected over a period of at least 10 min for each sample charge to ensure that stable particle sizes (as indicated by infrared scattering) and compositions (as discussed in section 2.2) were achieved. Typical particle number densities in
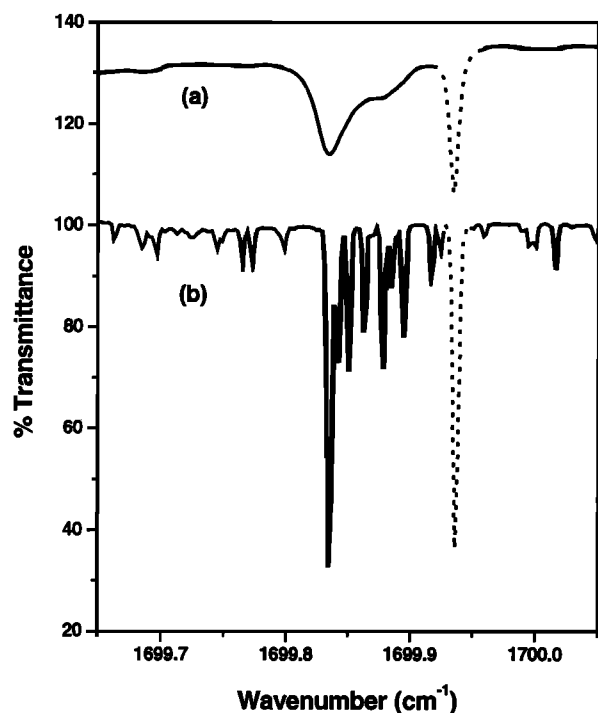
Figure 2. Experimental TDL spectra showing both nitric acid (solid curve) and water (dotted curve) transitions. (a) Spectrum (offset for clarity) recorded at 220 K with 100 torr helium buffer and in the presence of 70 wt % HNO₃ aerosols. (b) Spectrum recorded at room temperature with no helium buffer gas.

these experiments, controlled by varying total flow rates and cell pressures, were 10^4 - 10^6 particles cm⁻³, as determined from the Mie scattering calculations.

2.2. Aerosol Composition Determination

A major impediment to obtaining accurate optical constants for binary and ternary systems at low temperatures is the difficulty associated with characterizing the aerosol compositions. This is particularly an issue in the present case, given that the particles quickly equilibrate with any changes in the surrounding temperature or vapor pressures. Indeed, the diffusion of vapor phase species to the flow cell walls is quite rapid, and only after the wall interior is passivated (typically 1 – 2 min) can true particle-vapor equilibrium be maintained. In view of this, an in situ method of determining the particle composition has been developed in our laboratory [*Niedziela et al.*, 1999], which is based on the real-time measurement of the equilibrium pressures of the surrounding vapors. To do this quantitatively, we have coupled a tunable diode laser (TDL) to our flow cell. The high sensitivity and resolution available with this approach provide accurate in situ vapor pressure (and hence aerosol composition) measurements. As shown in Figure 1, the TDL and FTIR beams were overlapped to ensure that the vapor pressures correspond to those in equilibrium with the aerosols.

This TDL system was used in recent experiments [*Niedziela et al.*, 1999] to determine sulfuric acid aerosol compositions by measuring equilibrium water vapor pressures and relating them to the liquid concentrations using the *Carslaw et al.* [1995] thermodynamic model. Although the

H₂SO₄ vapor pressures were too low to be measured in this way, it was not problematic, since the vapor pressure of a single component is sufficient to determine the composition of a binary liquid. The same is certainly true for the binary HNO₃/H₂O liquids considered here, but the nitric acid vapor pressures are well within the TDL detection limit at 220 K, allowing us to monitor both H₂O and HNO₃. This provided us with a double check of the aerosol composition and confirmed that particles in the flow cell are indeed equilibrated. These experiments also afforded us the opportunity to demonstrate the ability to simultaneously monitor two vapor phase species, which will be essential for the characterization of ternary H₂SO₄/HNO₃/H₂O aerosols in future experiments.

Simultaneous monitoring of the water and nitric acid vapors was achieved by scanning a single mode of the diode laser at 1 kHz over a 0.5 cm⁻¹ wide region near 1700 cm⁻¹. The spectral windows were chosen to contain rovibrational transitions associated with both species, specifically within the v₂ band (bending mode) of water and the v₂ band (antisymmetric NO₂ stretch) of nitric acid. The laser output was directed through a monochromator and double-passed through the flow cell to increase the sensitivity. The entire TDL beam path was evacuated to eliminate interference from atmospheric water vapor absorption. Each TDL spectrum, an example of which is shown in Figure 2, was collected by averaging a HgCdTe detector signal for 15 seconds.

As we have discussed in an earlier publication [*Niedziela et al.*, 1999], a relatively high pressure of buffer gas is necessary in these experiments to suspend the aerosol particles and to ensure that the vapor pressures measured in the lower portion of the cell are indeed determined by its temperature. However, determination of the vapor pressures is complicated by the collisional broadening of the TDL absorption lines by the background buffer gas. The magnitude of this broadening can be appreciated by comparing the two spectra in Figure 2. For the vapor pressure analysis to be quantitative, we needed to determine the temperature-dependent pressure broadening coefficients for both water and nitric acid. By combining these coefficients with other spectroscopic parameters from the HITRAN database [*Rothman et al.*, 1992], the pressure-broadened spectra could be fit to obtain the H₂O and HNO₃ partial pressures. These measured pressures were then used to determine the aerosol weight percents using the *Carslaw et al.* [1995] model. The compositions obtained using the two vapor pressures agreed to within ± 0.5 wt % HNO₃ in all cases. The absolute error (± 1 wt % HNO₃) is somewhat larger, owing to a small uncertainty in flow cell temperature. Broadening coefficients (γ), measurable vapor pressure ranges (p), center frequencies (v₀), and line strengths (S) for the major transitions employed in this analysis are listed in Table 1.

To account for the temperature dependence observed in the pressure-broadening coefficient data, we calculated the line widths using a method discussed in detail elsewhere [*Niedziela et al.*, 1999]. Briefly, the pressure-broadened line width is calculated from kinetic theory [*Goody*, 1995] by adjusting the molecular collision diameter (σ_He) for the helium buffer gas. The results of these calculations, together with our experimental data points, are plotted in Figure 3. Within experimental error, the measured pressure-broadening

Table 1. Spectroscopic Parameters for Rovibrational Lines in the v_2 Bending Mode of H_2O and the v_2 NO_2 Stretching Mode of HNO_3

p, torr	V_0, cm^{-1}	S at 296 K, cm^{-1} molecules^{-1} cm^{-2}	γ_{air} at 296 K, cm^{-1} atm^{-1}	γ_{He}, cm^{-1} atm^{-1}
		Bending Mode of H₂O		
$\geq 10^{-2}$	1699.567	5.967×10^{-21}	0.0720	0.0180[*]
$\leq 10^{-2}$	1699.934	2.526×10^{-19}	0.1020	0.0142[*]
		NO₂ Stretching Mode of HNO₃		
9.2×10^{-6}	1699.384	2.638×10^{-20}	0.1100	0.0667 (280)[†]
	1699.832	2.673×10^{-20}	0.1100	0.0715 (260)[†]
				0.0696 (240)[†]
				0.0740 (220)[†]

For nitric acid, only the strongest line in each of the two spectral windows is listed, and the same helium-broadening coefficients (γ_{He}) were used for all lines. The room temperature line strengths (S) and air-broadening coefficients (γ_{air}) were taken from the HITRAN database [Rothman et al., 1992], to which the reader is referred for more detailed information on the energy levels involved in these transitions. Note that the γ units of cm^{-1} atm^{-1} are listed to be consistent with HITRAN, and that 1 atm = 1.01×10^5 Pa.

[*] Value is at 220 K.
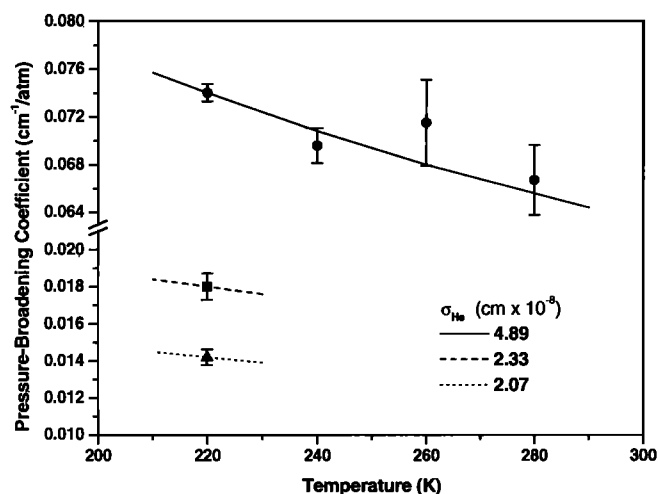
[†] Value is at (T, K).

coefficients exhibit the temperature dependence predicted from kinetic theory.

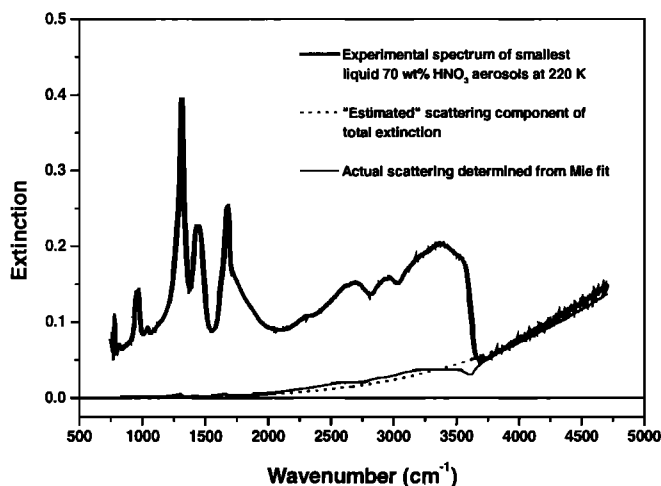### 2.3. Refractive Index Calculation

Frequency-dependent complex refractive indices for the liquid HNO_3 solutions were retrieved directly from FTIR aerosol extinction spectra using an iterative fitting procedure that we have applied to several other aerosol systems [Clapp et al., 1995; Richwine et al., 1995; Niedziela et al., 1998a,b]. Although the method has been described in detail elsewhere

Figure 3. A plot showing the temperature dependence of the helium pressure-broadening coefficients determined in the present study for nitric acid (solid circles), corresponding to the average value for all 40 transitions included in the fit, and for the 1699.567 cm^{-1} (solid square) and 1699.934 cm^{-1} (solid triangle) lines of water. The final values for the molecular collision diameter σ_{He} used to generate the curves are listed in the legend.

[Clapp et al., 1995; Niedziela et al., 1998a], a brief discussion is presented here, focusing on the modifications that were necessary for the present study. In this approach, the imaginary component $k(v)$ of the refractive index is first estimated, within an absolute scaling factor, from an extinction spectrum of small particles (< 0.1 μm radius) that to a first approximation, do not scatter infrared radiation [Bohren and Huffman, 1983]. The corresponding real component $n(v)$ is then calculated from $k(v)$ using a subtractive Kramers-Kronig transform [Bohren and Huffman, 1983]. Mie scattering theory is then used to simulate an experimental spectrum of large particles (> 0.5 μm radius) that do exhibit scattering, by averaging over a lognormal particle size distribution of median radius r_{med} and width σ. The resulting spectrum represents a unique interplay between the absorption and scattering processes [Clapp et al., 1995]. The calculated spectrum is then fit to the experimental data by adjusting the parameters associated with the size distribution and the $k(v)$ scaling factor. For each composition, optical constants were retrieved from a number of large particle spectra, spanning a range of sizes. The results obtained from the various data sets all agreed to within 3 %. The absolute error in $k(v)$ was ± 0.005 index units, limited primarily by a finite optical density at high frequencies. The accuracy of each data set was further tested by fitting several other experimental aerosol spectra with Mie theory to ensure they could be accurately simulated by varying only the r_{med} and σ size parameters.

A significant modification of the method was required for the present study, owing to the fact that small liquid HNO_3 particles (< 0.1 μm radius) could not be made without nucleating ice. As a result, we were unable to record truly nonscattering aerosol spectra, and our initial estimates of $k(v)$ had to be obtained using the method illustrated in Figure 4. Figure 4 shows that even for the smallest liquid particles we were able to make, there is still scattering at the highest frequencies. Nevertheless, since the scattering intensity I

Figure 4. The initial estimate for $k(v)$ obtained by subtracting the scattering component of the total extinction, estimated by fitting the high-frequency portion of the experimental spectrum (heavy solid curve) to v^4 (dotted curve). The actual scattering component (thin solid curve), determined from a Mie calculation based on our resulting 220 K, 70 wt % optical constants, is shown for comparison.

from these particles is related to the radiation frequency v by [*Ingle and Crouch*, 1988]

$$I(v) = av^4 \qquad (1)$$

in the absence of dispersion, we were able to subtract this component from the spectrum. The coefficient a was adjusted so that $I(v)$ (the dotted curve in Figure 4) overlapped the experimental spectrum at high frequencies. The corrected spectrum resulting from this subtraction was then used to initialize $k(v)$, as described above. Although scattering features associated with the dispersion within the vibrational resonances (particularly around 3600 cm⁻¹) were not properly accounted for in this way, these were dealt with later in the fitting procedure by periodically adjusting $k(v)$ to account for differences in the band shapes and positions between the calculated and experimental spectra [*Clapp et al.*, 1995; *Niedziela et al.*, 1998a]. This was necessary in any case, since the assumption that $k(v)$ is directly proportional to absorption is strictly valid only for bulk materials [*Bohren and Huffman*, 1983]. We have found empirically that as long as the large-particle spectrum has a strong enough scattering component, the fit converges to a unique solution for the complex refractive index [*Clapp et al.*, 1995]. To test the validity of this scattering correction, we applied it to spectra from our previous H₂SO₄/H₂O study [*Niedziela et al.*, 1998b]. The resulting data sets were in excellent agreement with our published data, the latter having been obtained by estimating $k(v)$ from truly nonscattering aerosol spectra.

Since the FTIR spectral range was limited by the 750 cm⁻¹ cutoff of the ZnS cell windows, it was necessary to deal with the truncation errors that occur in the subtractive Kramers-Kronig transform by splicing the data of *Querry and Tyler* [1980] from 400 to 780 cm⁻¹ to our $k(v)$. Since the data in this range was not adjusted during the fits, the present refractive indices are only reported down to 755 cm⁻¹. A similar procedure was used previously in our NAD and H₂SO₄

optical constant studies [*Niedziela et al.*, 1998a,b]. The subtractive Kramers-Kronig calculation also requires that a value of the real refractive index $n(v_o)$ be known at some frequency within the defined integration region [*Bohren and Huffman*, 1983]. Since the density of the liquid increases with decreasing temperature and the real index is a function of density [*Dale and Gladstone*, 1858], it was necessary to estimate this value at the temperature of interest. This was done by taking the room temperature value of $n(v_o)$ at 3800 cm⁻¹, obtained from linear interpolations of the 0.02 - 70 wt % HNO₃ data of Querry and Tyler and the water (0 wt % HNO₃) data of *Hale and Querry* [1973], and correcting them using the Lorentz-Lorenz formulation reported by *Beyerle et al.* [1997] to account for the density change associated with cooling to 220 K. The densities of the nitric acid solutions were estimated at 220 K using a formulation taken from *Carslaw et al.* [1995]. It is important to note here that any error in the anchor point $n(v_o)$ due to this interpolation-extrapolation method would result in a constant offset in the final $n(v)$ data, since the anchor point was chosen in a region where there are no vibrational resonances. The frequency-dependent shape, however, of the real index would not be affected [*Palmer et al.*, 1981].

3. Results and Discussion

We report here optical constants for supercooled nitric acid solutions of 34, 45, 54, 63, and 70 wt % at 220 K. Values for k and n at selected frequencies are listed for each data set in Table 2. In order to retrieve refractive indices at 220 K for compositions other than those studied, we have developed a FORTRAN routine that interpolates between the various data sets. The estimated error in the interpolated indices is comparable to the ± 3 % reported for the experimental data sets. To test the accuracy of this program, we have generated optical constants at intermediate compositions and used Mie theory to simulate supercooled aerosol spectra recorded in our flow cell. In all cases, the interpolated data gave residual differences of less than 0.2 % between the simulated and experimental spectra. The executable code of this program and ASCII files of the five complete data sets may be obtained directly from the authors or downloaded from our ftp site, ftp://frenchie.chem.unc.edu.

3.1. Room Temperature Versus 220 K Liquid Optical Constants

We begin our analysis of results by referring to Figure 5, which shows the refractive indices for 70 wt % HNO₃ at 220 K, compared with the corresponding room temperature data of *Querry and Tyler* [1980]. For this composition the data sets are in quite good agreement across the entire frequency range, the most obvious differences occurring in the O-H stretching region near 3300 cm⁻¹. Figure 5a shows that in the imaginary index data the positions and intensities of the v_8, v_5, v_4, and v_3 bands of molecular HNO₃ [*Querry and Tyler*, 1980] at 778, 949, 1304, and 1429 cm⁻¹, respectively, compare quite well between the two data sets. The same is true for the 1600 cm⁻¹ region, corresponding to the v_2 band of HNO₃ [*Querry and Tyler*, 1980] at 1672 cm⁻¹ and the v_2 bending mode of H₂O [*Querry and Tyler*, 1980] at 1640 cm⁻¹. Closer inspection of the data reveals some systematic trends. For example, the v_2 and v_1 bands of ionic NO₃⁻ [*Querry and*

Table 2. Selected Refractive Indices for the Five Supercooled HNO_3/H_2O Solution Compositions Reported Here at 220 K

ν, cm^{-1}	35 wt %		45 wt %		54 wt %		63 wt %		70 wt %	
	k	n	k	n	k	n	k	n	k	n
4700.82	0.000	1.340	0.000	1.350	0.003	1.360	0.002	1.364	0.001	1.367
4600.52	0.001	1.337	0.001	1.348	0.000	1.358	0.001	1.362	0.002	1.366
4500.21	0.001	1.335	0.001	1.344	0.002	1.356	0.002	1.359	0.002	1.364
4399.91	0.001	1.331	0.001	1.341	0.001	1.352	0.002	1.357	0.001	1.361
4299.60	0.002	1.326	0.001	1.337	0.001	1.348	0.002	1.354	0.003	1.359
4199.30	0.001	1.321	0.001	1.331	0.000	1.342	0.002	1.349	0.003	1.354
4100.92	0.001	1.315	0.001	1.325	0.001	1.336	0.002	1.344	0.004	1.351
4000.62	0.002	1.307	0.001	1.317	0.001	1.328	0.002	1.339	0.003	1.346
3900.31	0.002	1.296	0.001	1.306	0.001	1.317	0.002	1.331	0.002	1.340
3800.01	0.002	1.280	0.001	1.290	0.001	1.300	0.002	1.320	0.002	1.330
3699.70	0.002	1.250	0.002	1.260	0.004	1.268	0.002	1.297	0.002	1.311
3599.40	0.039	1.185	0.051	1.204	0.061	1.219	0.048	1.258	0.047	1.270
3549.24	0.089	1.182	0.094	1.206	0.100	1.231	0.076	1.274	0.072	1.292
3499.09	0.130	1.193	0.128	1.221	0.125	1.248	0.086	1.288	0.077	1.307
3475.95	0.147	1.201	0.143	1.229	0.135	1.256	0.090	1.292	0.079	1.311
3450.87	0.164	1.213	0.155	1.242	0.145	1.266	0.095	1.297	0.082	1.315
3425.79	0.179	1.228	0.168	1.254	0.154	1.278	0.101	1.303	0.084	1.320
3400.72	0.191	1.245	0.177	1.269	0.161	1.290	0.104	1.308	0.087	1.324
3375.64	0.199	1.263	0.183	1.285	0.166	1.304	0.107	1.315	0.089	1.329
3350.56	0.203	1.281	0.185	1.302	0.166	1.317	0.108	1.322	0.090	1.335
3325.49	0.204	1.296	0.185	1.315	0.165	1.328	0.109	1.328	0.089	1.339
3300.41	0.204	1.308	0.183	1.327	0.164	1.338	0.109	1.334	0.088	1.344
3275.34	0.206	1.321	0.183	1.339	0.160	1.348	0.108	1.338	0.088	1.346
3250.26	0.206	1.335	0.182	1.352	0.158	1.356	0.108	1.342	0.087	1.348
3225.18	0.205	1.349	0.177	1.361	0.156	1.364	0.107	1.346	0.087	1.351
3200.11	0.203	1.364	0.174	1.372	0.151	1.372	0.107	1.350	0.086	1.354
3175.03	0.197	1.379	0.166	1.382	0.145	1.379	0.105	1.354	0.085	1.356
3149.95	0.187	1.392	0.159	1.389	0.138	1.384	0.103	1.357	0.083	1.359
3124.88	0.176	1.402	0.152	1.395	0.132	1.388	0.100	1.360	0.082	1.360
3099.80	0.164	1.408	0.143	1.399	0.126	1.390	0.098	1.362	0.080	1.362
3049.65	0.145	1.414	0.130	1.404	0.114	1.391	0.092	1.364	0.073	1.360
2999.50	0.124	1.418	0.117	1.406	0.106	1.388	0.090	1.360	0.076	1.356
2949.35	0.110	1.408	0.102	1.406	0.100	1.383	0.093	1.362	0.078	1.355
2901.12	0.107	1.404	0.095	1.395	0.101	1.378	0.092	1.364	0.082	1.358
2850.97	0.105	1.402	0.096	1.390	0.100	1.377	0.089	1.364	0.079	1.359
2800.82	0.098	1.404	0.099	1.389	0.102	1.377	0.089	1.360	0.079	1.355
2750.66	0.094	1.402	0.097	1.391	0.103	1.377	0.095	1.358	0.088	1.353
2700.51	0.089	1.402	0.094	1.393	0.103	1.380	0.100	1.363	0.094	1.358
2650.36	0.084	1.400	0.090	1.393	0.101	1.381	0.101	1.369	0.096	1.366
2600.21	0.079	1.396	0.086	1.392	0.099	1.381	0.101	1.373	0.096	1.372
2550.06	0.076	1.392	0.083	1.389	0.095	1.380	0.098	1.377	0.092	1.377
2499.90	0.073	1.386	0.081	1.383	0.094	1.376	0.094	1.378	0.088	1.379
2449.75	0.074	1.381	0.082	1.380	0.094	1.373	0.092	1.377	0.084	1.380
2399.60	0.075	1.377	0.084	1.377	0.095	1.369	0.089	1.375	0.081	1.378
2349.45	0.078	1.376	0.086	1.376	0.098	1.367	0.089	1.371	0.079	1.374
2301.22	0.078	1.373	0.084	1.377	0.099	1.365	0.091	1.370	0.081	1.373
2249.14	0.078	1.369	0.083	1.369	0.100	1.360	0.090	1.370	0.078	1.373
2200.92	0.079	1.366	0.086	1.363	0.103	1.356	0.087	1.367	0.075	1.369
2150.77	0.081	1.363	0.091	1.361	0.104	1.352	0.086	1.362	0.072	1.363
2100.61	0.082	1.359	0.094	1.358	0.107	1.346	0.087	1.354	0.073	1.355
2050.46	0.083	1.354	0.097	1.354	0.112	1.338	0.091	1.346	0.077	1.346

Table 2. (continued)

v, cm⁻¹	35 wt %		45 wt %		54 wt %		63 wt %		70 wt %	
	k	n	k	n	k	n	k	n	k	n
2000.31	0.084	1.347	0.100	1.348	0.120	1.330	0.096	1.338	0.081	1.337
1950.16	0.090	1.336	0.106	1.339	0.131	1.319	0.104	1.328	0.088	1.327
1900.00	0.103	1.325	0.119	1.331	0.150	1.310	0.119	1.319	0.102	1.317
1849.85	0.118	1.321	0.137	1.329	0.173	1.310	0.137	1.316	0.118	1.313
1799.70	0.136	1.320	0.153	1.333	0.195	1.316	0.153	1.316	0.131	1.311
1749.55	0.152	1.328	0.163	1.339	0.213	1.330	0.171	1.318	0.142	1.306
1699.39	0.168	1.334	0.185	1.345	0.229	1.335	0.200	1.298	0.188	1.260
1649.24	0.195	1.361	0.207	1.369	0.251	1.398	0.238	1.410	0.242	1.406
1599.09	0.146	1.396	0.164	1.408	0.177	1.414	0.152	1.419	0.148	1.423
1575.94	0.128	1.378	0.142	1.389	0.155	1.380	0.128	1.387	0.116	1.391
1550.87	0.118	1.353	0.134	1.362	0.152	1.337	0.122	1.349	0.107	1.350
1539.29	0.119	1.343	0.136	1.351	0.158	1.318	0.124	1.330	0.108	1.331
1529.65	0.118	1.330	0.134	1.339	0.163	1.299	0.128	1.312	0.112	1.313
1520.00	0.120	1.318	0.137	1.326	0.174	1.279	0.137	1.294	0.121	1.294
1510.36	0.124	1.302	0.141	1.312	0.191	1.258	0.151	1.275	0.134	1.275
1500.71	0.132	1.289	0.147	1.298	0.215	1.240	0.172	1.260	0.153	1.260
1489.14	0.145	1.270	0.158	1.276	0.253	1.226	0.203	1.247	0.184	1.247
1479.49	0.161	1.254	0.174	1.255	0.290	1.223	0.233	1.246	0.212	1.246
1469.85	0.184	1.242	0.199	1.234	0.328	1.229	0.263	1.252	0.239	1.251
1460.21	0.212	1.235	0.241	1.220	0.368	1.249	0.291	1.267	0.262	1.265
1450.56	0.244	1.237	0.283	1.230	0.395	1.283	0.312	1.290	0.282	1.282
1440.92	0.273	1.247	0.318	1.245	0.412	1.317	0.327	1.317	0.298	1.303
1429.34	0.302	1.267	0.353	1.278	0.418	1.362	0.331	1.352	0.306	1.336
1419.70	0.327	1.286	0.369	1.310	0.409	1.396	0.322	1.381	0.302	1.363
1410.05	0.337	1.327	0.375	1.343	0.388	1.422	0.301	1.402	0.284	1.385
1400.41	0.331	1.347	0.368	1.373	0.361	1.435	0.273	1.407	0.261	1.392
1390.76	0.321	1.364	0.350	1.387	0.334	1.428	0.248	1.398	0.234	1.389
1384.98	0.316	1.365	0.340	1.387	0.325	1.416	0.236	1.384	0.220	1.378
1379.19	0.314	1.363	0.340	1.382	0.322	1.403	0.231	1.368	0.212	1.362
1375.33	0.318	1.360	0.341	1.381	0.322	1.394	0.228	1.358	0.208	1.351
1369.55	0.323	1.359	0.343	1.375	0.327	1.379	0.229	1.338	0.209	1.330
1365.69	0.330	1.360	0.348	1.371	0.333	1.370	0.234	1.324	0.212	1.316
1359.90	0.345	1.363	0.362	1.366	0.348	1.358	0.243	1.307	0.223	1.299
1357.97	0.347	1.366	0.368	1.365	0.354	1.355	0.246	1.300	0.225	1.295
1354.11	0.357	1.372	0.382	1.366	0.368	1.351	0.257	1.285	0.230	1.280
1348.33	0.369	1.384	0.406	1.376	0.392	1.350	0.290	1.272	0.250	1.261
1344.47	0.375	1.394	0.420	1.389	0.406	1.354	0.299	1.271	0.264	1.247
1340.61	0.383	1.405	0.428	1.403	0.420	1.358	0.311	1.265	0.282	1.236
1334.82	0.389	1.428	0.441	1.426	0.441	1.368	0.334	1.250	0.311	1.220
1330.97	0.391	1.442	0.445	1.442	0.454	1.376	0.355	1.240	0.337	1.207
1325.18	0.390	1.468	0.447	1.466	0.472	1.389	0.401	1.227	0.398	1.194
1319.39	0.385	1.492	0.447	1.490	0.497	1.405	0.467	1.227	0.475	1.208
1315.54	0.375	1.508	0.445	1.505	0.515	1.419	0.522	1.248	0.529	1.243
1309.75	0.357	1.525	0.441	1.527	0.543	1.456	0.591	1.323	0.581	1.331
1305.89	0.348	1.535	0.439	1.543	0.554	1.490	0.607	1.393	0.587	1.396
1300.10	0.329	1.546	0.429	1.568	0.547	1.547	0.583	1.484	0.560	1.479
1294.32	0.309	1.552	0.410	1.589	0.522	1.589	0.535	1.536	0.512	1.528
1290.46	0.298	1.554	0.398	1.599	0.503	1.608	0.508	1.553	0.483	1.546
1280.81	0.273	1.552	0.367	1.620	0.459	1.639	0.457	1.579	0.428	1.565
1269.24	0.252	1.546	0.333	1.626	0.414	1.659	0.416	1.600	0.388	1.575
1259.60	0.240	1.543	0.311	1.631	0.382	1.669	0.382	1.609	0.364	1.589

Table 2. (continued)

| v, cm⁻¹	35 wt %		45 wt %		54 wt %		63 wt %		70 wt %	
	k	n	k	n	k	n	k	n	k	n
1249.95	0.230	1.536	0.291	1.636	0.349	1.675	0.350	1.617	0.333	1.595
1240.31	0.221	1.531	0.272	1.640	0.317	1.677	0.323	1.615	0.309	1.596
1230.66	0.216	1.526	0.246	1.641	0.288	1.672	0.301	1.614	0.286	1.596
1219.09	0.209	1.523	0.218	1.629	0.258	1.659	0.278	1.607	0.262	1.591
1209.44	0.206	1.520	0.208	1.616	0.239	1.644	0.263	1.601	0.246	1.585
1199.80	0.202	1.516	0.201	1.607	0.227	1.627	0.252	1.594	0.233	1.577
1190.15	0.200	1.514	0.194	1.598	0.221	1.611	0.242	1.587	0.224	1.570
1180.51	0.197	1.512	0.190	1.592	0.219	1.599	0.235	1.580	0.215	1.564
1170.86	0.194	1.511	0.186	1.586	0.219	1.590	0.229	1.575	0.208	1.557
1159.29	0.192	1.508	0.182	1.582	0.220	1.584	0.223	1.570	0.202	1.550
1149.65	0.191	1.508	0.179	1.578	0.219	1.582	0.219	1.565	0.196	1.543
1140.00	0.190	1.506	0.176	1.575	0.216	1.579	0.215	1.561	0.194	1.539
1130.36	0.187	1.506	0.172	1.573	0.211	1.575	0.212	1.557	0.190	1.533
1120.71	0.185	1.506	0.169	1.569	0.209	1.570	0.208	1.554	0.189	1.529
1111.07	0.183	1.506	0.166	1.565	0.208	1.566	0.206	1.551	0.186	1.526
1099.49	0.179	1.504	0.164	1.561	0.208	1.564	0.202	1.547	0.183	1.521
1089.85	0.178	1.502	0.162	1.558	0.207	1.559	0.199	1.545	0.179	1.517
1080.20	0.174	1.502	0.160	1.555	0.205	1.556	0.195	1.539	0.176	1.511
1070.56	0.170	1.498	0.157	1.549	0.203	1.551	0.192	1.534	0.174	1.507
1060.92	0.167	1.490	0.156	1.543	0.198	1.540	0.189	1.524	0.171	1.495
1049.34	0.179	1.478	0.171	1.532	0.216	1.524	0.199	1.510	0.182	1.481
1045.48	0.188	1.483	0.178	1.538	0.225	1.528	0.207	1.509	0.188	1.480
1039.70	0.190	1.494	0.179	1.549	0.231	1.541	0.213	1.514	0.193	1.486
1035.84	0.185	1.500	0.175	1.555	0.229	1.549	0.215	1.519	0.193	1.488
1030.05	0.178	1.501	0.167	1.558	0.222	1.553	0.211	1.524	0.189	1.490
1024.27	0.173	1.500	0.163	1.556	0.214	1.555	0.205	1.524	0.185	1.488
1020.41	0.172	1.499	0.160	1.556	0.209	1.552	0.203	1.522	0.182	1.485
1010.76	0.167	1.497	0.154	1.553	0.204	1.544	0.199	1.513	0.178	1.473
1001.12	0.161	1.492	0.150	1.547	0.203	1.534	0.199	1.500	0.180	1.455
991.47	0.160	1.484	0.149	1.541	0.207	1.523	0.210	1.482	0.194	1.433
979.90	0.160	1.479	0.151	1.535	0.224	1.513	0.240	1.468	0.231	1.413
970.26	0.162	1.475	0.154	1.533	0.245	1.518	0.278	1.474	0.280	1.416
960.61	0.163	1.471	0.156	1.534	0.256	1.537	0.311	1.506	0.325	1.452
954.82	0.164	1.468	0.156	1.535	0.255	1.551	0.321	1.536	0.339	1.487
950.97	0.164	1.467	0.155	1.536	0.251	1.562	0.320	1.557	0.341	1.512
945.18	0.165	1.464	0.153	1.536	0.237	1.572	0.308	1.588	0.332	1.549
939.39	0.166	1.462	0.151	1.534	0.221	1.569	0.284	1.609	0.310	1.579
935.53	0.166	1.460	0.150	1.533	0.213	1.564	0.265	1.615	0.290	1.591
929.75	0.167	1.457	0.148	1.529	0.208	1.558	0.242	1.616	0.260	1.598
920.10	0.170	1.451	0.149	1.524	0.205	1.546	0.216	1.603	0.225	1.590
910.46	0.175	1.445	0.151	1.518	0.205	1.535	0.204	1.590	0.206	1.576
908.53	0.176	1.443	0.152	1.518	0.205	1.534	0.203	1.589	0.202	1.572
900.81	0.182	1.439	0.154	1.515	0.208	1.529	0.197	1.580	0.197	1.560
881.52	0.195	1.432	0.161	1.509	0.216	1.516	0.192	1.566	0.188	1.544
860.31	0.214	1.425	0.174	1.503	0.232	1.502	0.189	1.553	0.182	1.530
839.09	0.245	1.413	0.192	1.495	0.257	1.488	0.192	1.537	0.178	1.505
819.80	0.278	1.459	0.211	1.524	0.299	1.528	0.214	1.538	0.200	1.491
800.51	0.281	1.458	0.208	1.521	0.286	1.521	0.205	1.525	0.199	1.467
779.29	0.302	1.486	0.222	1.537	0.335	1.572	0.276	1.543	0.306	1.476
765.79	0.303	1.501	0.222	1.545	0.281	1.595	0.234	1.571	0.253	1.529
754.21	0.302	1.512	0.222	1.552	0.263	1.577	0.216	1.559	0.240	1.520
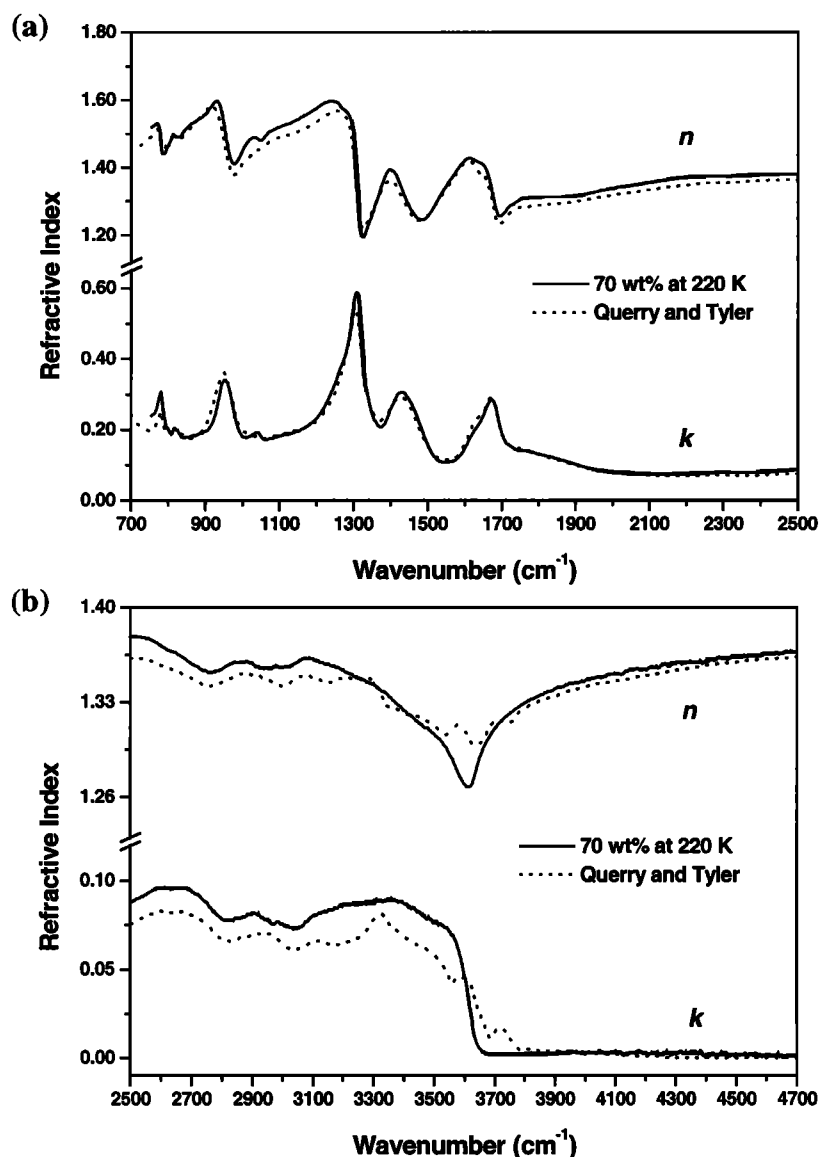
Figure 5. Comparisons of the present 70 wt % HNO₃ optical constants at 220 K (solid curves) with those of *Querry and Tyler* [1980] for room temperature bulk solutions (dotted curves). (a) Expanded view from 700 to 2500 cm⁻¹. (b) Expanded view from 2500 to 4700 cm⁻¹.

Tyler, 1980; *Ritzhaupt and Devlin*, 1977] at 820 and 1040 cm⁻¹ are slightly more intense in the 220 K data, while conversely, the molecular HNO₃ bands are slightly weaker. As mentioned above, the largest differences occur from 2500 to 3600 cm⁻¹ (Figure 5b), where absorptions from H₂O and H₃O⁺ dominate [*Querry and Tyler*, 1980]. In this case, the low-temperature $k(v)$ is smoother and more intense. The irregular shape of the Querry and Tyler data in this region leads us to suspect problems with the room temperature imaginary indices. Indeed, the uncertainty quoted for this $k(v)$ data is ± 0.02 for values > 0.05 and even greater with smaller $k(v)$ values [*Querry and Tyler*, 1980]. Figure 6 depicts Mie simulations of a 220 K aerosol spectrum using both the Querry and Tyler data set and the one reported here. Though both fits converge to similar size distributions, the room temperature data result in a relatively poor fit in the 2300 - 3600 cm⁻¹ region, as expected.

For more dilute nitric acid concentrations we see even more significant differences, as illustrated in Figures 7a and

7b, which compare the present 35 wt %, 220 K refractive indices with the corresponding room temperature results [*Querry and Tyler*, 1980]. It is evident in Figure 7a that the low-temperature data set exhibits strong NO₃⁻ bands at 820 and 1040 cm⁻¹, while the *Querry and Tyler* [1980] data is dominated by HNO₃ absorption at 949 cm⁻¹. In addition, the intensity of the v_3 NO₃⁻ doublet, centered at 1350 cm⁻¹ [*Querry and Tyler*, 1980; *Ritzhaupt and Devlin*, 1977], is greater in the 220 K data set. Although it is difficult to quantify the relative contributions to these $k(v)$ data from the nitrate ion and molecular nitric acid at 1304 and 1429 cm⁻¹, respectively, the results certainly indicate that the equilibrium shifts from molecular HNO₃ to ionic NO₃⁻ as the temperature is lowered.

Here again the differences are more pronounced in the 3300 cm⁻¹ region, highlighted in Figure 7b. The broad O-H stretch in the 220 K $k(v)$ data is considerably more intense and is shifted to the red by 40 cm⁻¹, with respect to the 300 K data. This phenomenon is directly analogous to what we
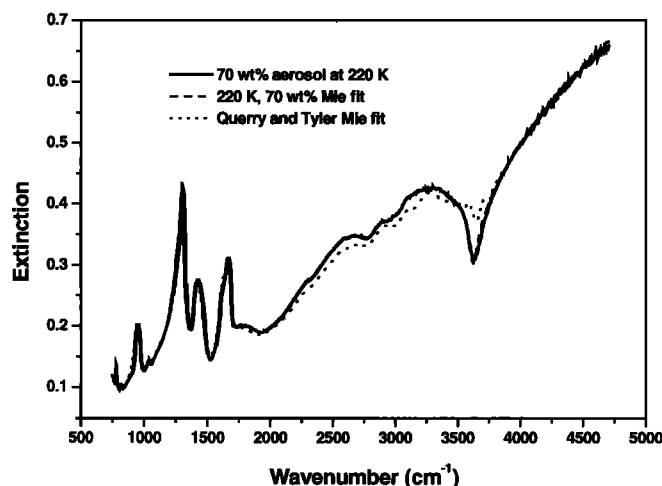
Figure 6. A comparison of the quality of Mie fits to an aerosol spectrum obtained using the two data sets in Figure 5. The resulting size distribution parameters are $r_{med} = 0.63$ μm and $\sigma = 0.46$ using the present data (dashed curve) and $r_{med} = 0.61$ μm and $\sigma = 0.49$ using the *Querry and Tyler* [1980] data (dotted curve).

observed in the binary H_2SO_4/H_2O liquid [*Niedziela et al.*, 1998b], where the equilibrium between bisulfate and sulfate ion shifted to the doubly charged SO_4^{-2} upon cooling. In comparing our 38 wt % H_2SO_4 refractive index data at 220 K with the room temperature data of *Palmer and Williams* [1975], we attributed the increased intensity and the lowered energy of the O-H stretch to stronger hydrogen bonding between H_2O and SO_4^{-2}, compared with HSO_4^-. We argue the same case here, except that we now consider the equilibrium shift between molecular HNO_3 and singly charged NO_3^-. The effect is somewhat weaker in the present case, as the red shift for the 35 wt % nitric acid solution is approximately 0.5 cm⁻¹ K⁻¹, compared to 1 cm⁻¹ K⁻¹ for 38 wt % sulfuric acid [*Niedziela et al.*, 1998b]. On the other hand, it is large compared to the 0.2 cm⁻¹ K⁻¹ shift reported by *Clapp et al.* [1995] for pure water ice, where ion-water interactions are absent. As a result of the significant differences between the room temperature and 220 K data at this nitric acid concentration, Mie fits to supercooled aerosol spectra using the 300 K data are very poor, as shown in Figure 8, and result in a 20 % overestimation of particle size.

3.2. Liquid Versus Amorphous Solid Optical Constants

In this section we compare the refractive indices for 63 and 54 wt % HNO_3 solutions at 220 K with those of amorphous solid solutions of the same stoichiometries. Specifically, we refer to the *Toon et al.* [1994] data for amorphous NAD and NAT (henceforth referred to as a-NAD and a-NAT) thin film optical constants at < 160 K. It is immediately clear in Figure 9 that there are significant differences between the liquid and solid data sets at 63 wt %. We note that for both compositions the amorphous solid data exhibit stronger nitrate ion absorptions at 820 and 1040 cm⁻¹ and weaker molecular nitric acid bands at 778, 949, and 1672 cm⁻¹. In addition, the 3300 cm⁻¹ O-H stretch is red-shifted by approximately 100 cm⁻¹ and is more intense compared to the 220 K liquid data.

Given these differences, it is interesting to consider the consequences of using the amorphous solid optical constants to simulate supercooled liquid aerosol spectra. As pointed out above, *Toon et al.* [1994] assumed in an earlier study that the optical constants for supercooled liquid HNO_3 were the same as the amorphous solid of the same composition. This seemed justified, given that *Ritzhaupt and Devlin* [1991] and *Koehler et al.* [1992] have reported similarities in the infrared spectra of the two phases. However, in a crystallization study of NAD aerosols, *Disselkamp et al.* [1996] used the a-NAD optical constants to simulate the extinction spectra of 193 K particles, assumed to have a $H_2O:HNO_3$ stoichiometry of 2:1. The fits were generally poor, as the calculated spectra had stronger NO_3^- and H_3O^+ features, correspondingly weaker HNO_3 absorptions, and the O-H band was shifted red by about 100 cm⁻¹. The authors attributed these discrepancies to differences in composition, temperature, and phase of their aerosols, compared to the solid thin films from which the optical constants were derived. They also suggested that the aerosol size distribution used in their analysis might not be quantitatively representative of the actual aerosol. Given the data presented here, it is now clear that these discrepancies are due to differences in the optical constants.

Figure 10 shows the simulations of a 64 wt % supercooled liquid HNO_3 aerosol spectrum using both the 220 K liquid and the < 160 K solid solution [*Toon et al.*, 1994] optical constants. The FTIR spectrum was collected in our flow cell at 190 K so that we could duplicate the *Disselkamp et al.* [1996] results. It is immediately clear that the liquid data produce an excellent fit, while the a-NAD fit is poor. In particular, the solid data overestimate the NO_3^- band intensities at 820 and 1040 cm⁻¹ and underestimate the HNO_3 features at 778 and 949 cm⁻¹. The O-H band near 3300 cm⁻¹ is red-shifted by approximately 100 cm¹, and the fit from 1600 to 3300 cm⁻¹ is too intense. These discrepancies are identical to those reported by Disselkamp et al. in their Mie simulations. Since the Mie calculations in the present work also employ a single log-normal size distribution, it is not likely that this is a major source of error, given how well the liquid data fit the spectrum in Figure 10. The differences are largely attributed to the same kind of ionic equilibrium shift with temperature as that which occurs in the liquid. This results in increased concentrations of nitrate and hydronium ions in the low-temperature solid and correspondingly less molecular HNO_3, compared to the higher-temperature liquid solution.

The most significant error that results from using the amorphous solid optical constants in fitting the supercooled liquid aerosol spectra is associated with the particle size that is obtained. As listed in the Figure 10 caption, the median radius (r_{med}) determined from the Mie fit based on the amorphous solid data is 2.6 times larger than that obtained using the optical constants from this work. This is important because *Disselkamp et al.* [1996] used the amorphous solid data to derive particle sizes in their study of the crystallization rate of liquid nitric acid, which is inversely related to the particle volume. As a consequence, the associated error would be an underestimation of the crystallization rate by a factor of $(2.6)^3$, or 17.6. We have not reanalyzed the Disselkamp et al. data in light of the present results, but such a review is clearly warranted.
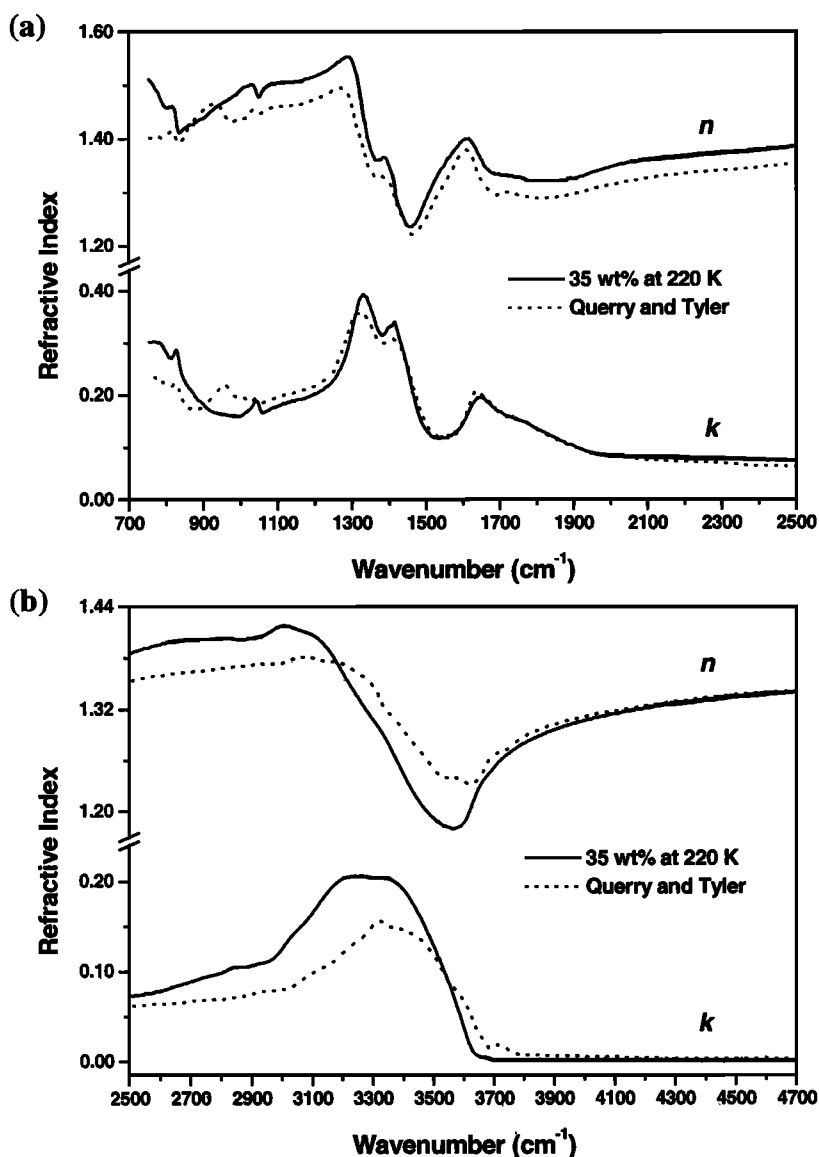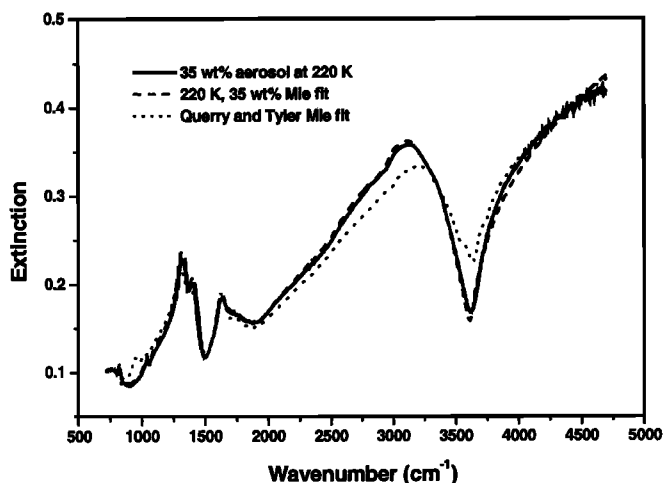
(a)

(b)

Figure 7. Comparisons of the present 35 wt % HNO₃ optical constants at 220 K (solid curves) with those of *Querry and Tyler* [1980] for room temperature bulk solutions (dotted curves). (a) Expanded view from 700 to 2500 cm⁻¹. (b) Expanded view from 2500 to 4700 cm⁻¹.


3.3. Nitric Acid Dissociation

The spectral evidence presented here suggests that molecular nitric acid is not fully dissociated above 35 wt % and that cooling a solution promotes the formation of NO_3^- and H_3O^+ ions. We recently presented a discussion of an analogous dissociation phenomenon in the binary H_2SO_4/H_2O system [*Niedziela et al.*, 1998b], in which we quantified the relative amounts of bisulfate (HSO_4^-) and sulfate (SO_4^{-2}) ions

Figure 8. A comparison of the quality of Mie fits to an aeros.· spectrum obtained using the two data sets in Figure 7. The resulting size distribution parameters are r_{med} = 0.65 μm and σ = 0.52 using the present data (dashed curve), and r_{med} = 0.77 μm and σ = 0.51 using the *Querry and Tyler* [1980] data (dotted curve).

(a)

(b)
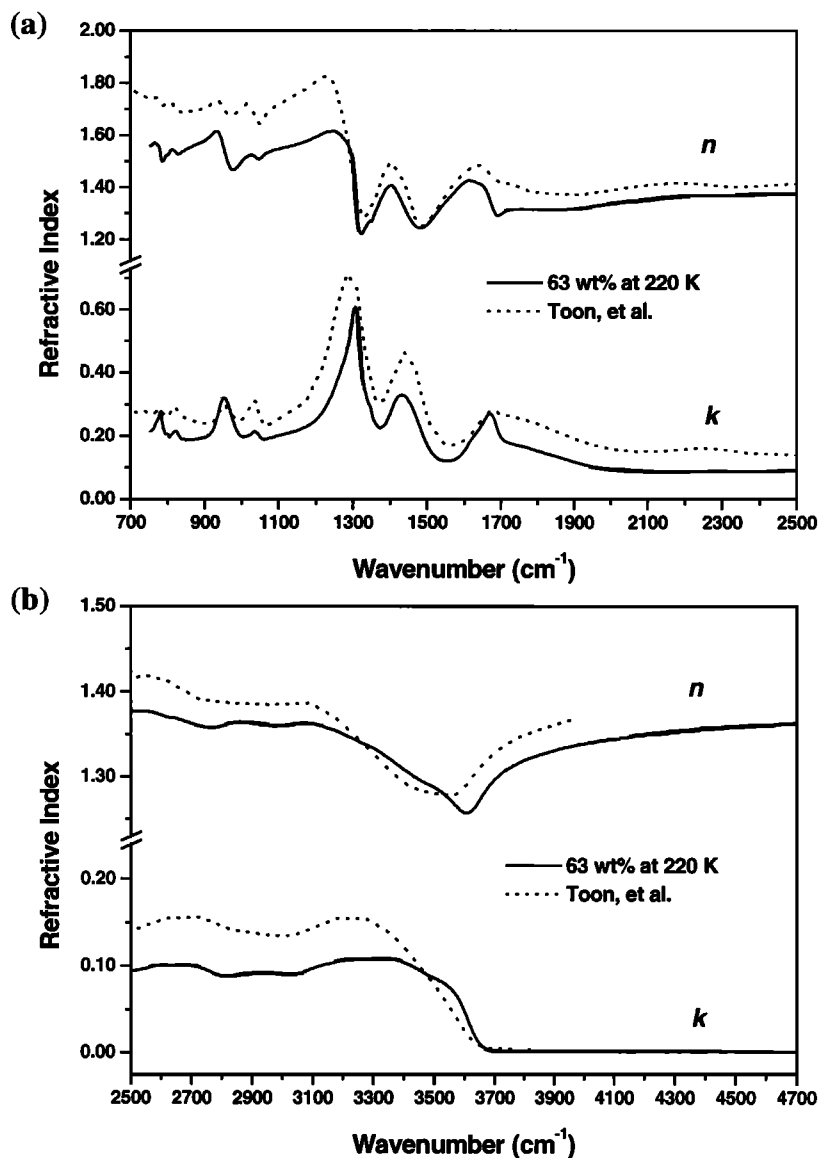
Figure 9. Comparisons of optical constants derived from 63 wt %, 220 K supercooled liquid HNO₃ aerosols in this study (solid curves) with those of < 160 K a-NAD thin films from *Toon et al.* [1994] (dotted curves). (a) Expanded view from 700 to 2500 cm⁻¹. (b) Expanded view from 2500 to 4700 cm⁻¹.
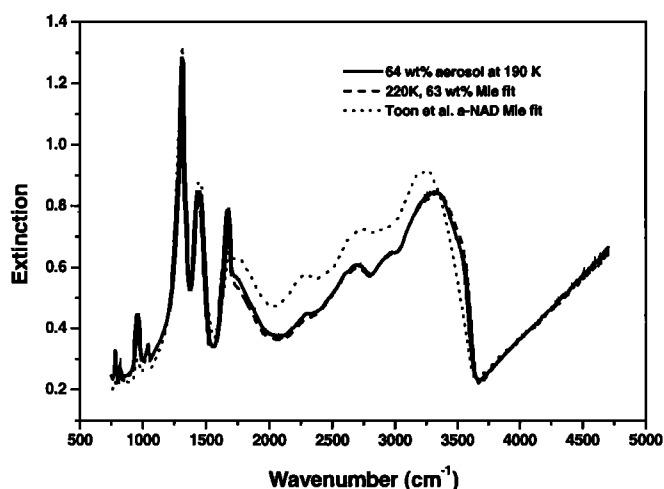

in solution using the *Carslaw et al.* [1995] model. Since that same model assumes complete dissociation of HNO₃ at all compositions and temperatures [*Carslaw et al.*, 1995], we must refer to the associated solution thermodynamics for this discussion of this issue. As an aside, we can still confidently employ the Carslaw et al. model for HNO₃ aerosol composition determinations, since it represents an extensive parameterization of laboratory vapor pressure measurements over a wide range of temperatures and compositions [*Carslaw*

Figure 10. Mie fits to a spectrum (solid) of supercooled 64 wt % HNO₃ aerosols at 190 K. The 220 K optical constant data simulate the spectrum quite well (dashed curve) with r_{med} = 0.16 μm and σ = 0.53, while the a-NAD data [*Toon et al.*, 1994] result in a poor fit (dotted curve) with r_{med} = 0.41 μm and σ = 0.15.

et al., 1995], including those of *Hanson and Mauersberger* [1988b] for supercooled HNO₃ solutions.

Experimental values for the degree of dissociation (α) of molecular HNO₃, related to the thermodynamic equilibrium constant K_a,

$$HNO_3 + H_2O \xleftrightarrow{K_a} NO_3^- + H_3O^+ , \qquad (2)$$
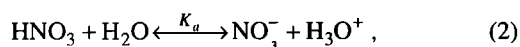
have been determined by several methods at room temperature [*Young et al.*, 1959; *Davis and DeBruin*, 1964]. Of particular interest here is a ¹H nuclear magnetic resonance (NMR) study by *Hood and Reilly* [1960], in which nitric acid dissociation was studied at 0°, 25°, and 70°C. Their work showed that when cooling a solution of 70 wt % HNO₃ from room temperature to 0°C, α increases from 0.151 to 0.176. For a 35 wt % solution the corresponding increase was larger, specifically from 0.632 to 0.710. Although no such investigations have been carried out below the water freezing point, our spectroscopic data suggest that the trend continues to 220 K. This is consistent with the van't Hoff equation,

$$\frac{d \ln K}{dT} = \frac{\Delta_r H^\circ}{RT^2} , \qquad (3)$$

which indicates that for an exothermic process like HNO₃ dissolution, the equilibrium constant (K) increases with decreasing temperature [*Atkins*, 1994]. Certainly, this effect would be greater for the more dilute solutions, as is seen in our data and indicated by the NMR results.

4. Summary

Frequency-dependent infrared complex refractive indices have been reported for the first time for supercooled liquid HNO₃/H₂O aerosols at 220 K. Differences between these new data sets and those of room temperature bulk liquid solutions and < 160 K amorphous solid thin films have been attributed primarily to temperature-dependent dissociation of molecular HNO₃ into its constituent ions. In simulating supercooled aerosol spectra we have shown that the low-temperature amorphous solid optical constants give particle sizes in error by a factor of 2 or more. Consequently, these new data sets should provide a more accurate analysis of nitric acid aerosol spectra collected in both remote sensing and laboratory experiments. The results for binary HNO₃/H₂O are directly analogous to previous studies of the binary H₂SO₄/H₂O system, ultimately pointing the way to future investigations of ternary PSC aerosol refractive indices.

References

Arnold, F, Stratospheric aerosol increases and ozone destruction: Implications from mass spectrometer measurements, *Ber. Bunsen Ges. Phys. Chem.*, *96*, 339-350, 1992.

Atkins, P.W., *Physical Chemistry*, W. H. Freeman, New York, 1994.

Bertram, A. K , and J. J. Sloan, Temperature-dependent nucleation rate constants and freezing behavior of submicron nitric acid dihydrate aerosol particles under stratospheric conditions, *J. Geophys. Res.*, *103*, 3553-3561, 1998.

Beyerle, G , B. P. Luo, R. Neuber, T. Peter, and I. S McDermid, Temperature dependence of ternary solution particle volumes as observed by lidar in the Arctic stratosphere during winter 1992/1993, *J. Geophys. Res.*, *102*, 3603-3609, 1997.

Bohren, C F, and D. R. Huffman, *Absorption and Scattering of Light by Small Particles*, John Wiley, New York, 1983

Boone, T. L., K. A. Fuller, and H. D. Downing, Infrared optical constants of aqueous solutions of nitric acid, *J. Phys. Chem.*, *84*, 2666-2667, 1980.

Carslaw, K. S., B P. Luo, S. L. Clegg, T. Peter, P. Brimblecombe, and P J. Crutzen, Stratospheric aerosol growth and HNO₃ gas phase depletion from coupled HNO₃ and water uptake by liquid particles, *Geophys. Res. Lett.*, *21*, 2479-2482, 1994.

Carslaw, K. S., S. L. Clegg, and P. Brimblecombe, A thermodynamic model of the system HCl-HNO₃-H₂SO₄-H₂O, including solubilities of HBr, from < 200 to 328 K, *J. Phys. Chem.*, *99*, 11,557-11,574, 1995.

Clapp, M. L., R E. Miller, and D. R. Worsnop, Frequency dependent optical constants of water ice obtained directly from aerosol extinction spectra, *J. Phys. Chem.*, *99*, 6317-6326, 1995.

Dale, T P , and J. H. Gladstone, On the influence of temperature on the refraction of light, *Phil. Trans. R. Soc. London*, *148*, 887-894, 1858.

Davis, W, Jr., and H. J. DeBruin, New activity coefficients of 0-100 per cent aqueous nitric acid, *J. Inorg. Nucl. Chem.*, *26*, 1069-1083, 1964.

Disselkamp, R S., S. E. Anthony, A. J. Prenni, T. B. Onsach, and M. A. Tolbert, Crystallization kinetics of nitric acid dihydrate aerosols, *J. Phys. Chem.*, *100*, 9127-9137, 1996.

Drdla, K., A. Tabazadeh, R P. Turco, M. Z. Jacobson, J. E. Dye, C. Twohy, and D. Baumgardner, Analysis of the physical state of one arctic polar stratospheric cloud based on observations, *Geophys. Res. Lett.*, *21*, 2475-2478, 1994.

Goody, R., *Principles of Atmospheric Physics and Chemistry*, Oxford Univ. Press, New York, 1995.

Hale, G M., and M. R. Querry, Optical constants of water in the 200 nm to 200 μm wavelength region, *Appl. Opt.*, *12*, 555-563, 1973.

Hanson, D., and K. Mauersberger, Laboratory studies of the nitric acid trihydrate: Implications for the South Polar stratosphere, *Geophys. Res. Lett.*, *15*, 855-858, 1988a.

Hanson, D. R. and K Mauersberger, Vapor pressures of HNO₃/H₂O solutions at low temperatures, *J. Phys. Chem.*, *92*, 6167-6170, 1988b.

Hood, G. C., and C. A. Reilly, Ionization of strong electrolytes, VIII, Temperature coefficient of dissociation of strong acids by proton magnetic resonance, *J. Chem. Phys.*, *32*, 127-130, 1960.

Ingle, J. D., and S. R. Crouch, *Spectrochemical Analysis*, Prentice-Hall, Englewood Cliffs, N.J., 1988.

Kinne, S., O. B. Toon, G. C. Toon, C. B. Farmer, E. V. Browell, and M. P. McCormick, Measurements of size and composition of particles in polar stratospheric clouds from infrared solar absorption spectra, *J. Geophys. Res.*, *94*, 16,481-16,491, 1989.

Koehler, B. G., A. M. Middlebrook, and M. A. Tolbert, Characterization of model polar stratospheric cloud films using Fourier transform infrared spectroscopy and temperature programmed desorption, *J. Geophys. Res.*, *97*, 8065-8074, 1992.

McDonald, J. E., Homogeneous nucleation of vapor condensation, I, Thermodynamic aspects, *Am. J. Phys.*, *30*, 870-877, 1962.

Molina, M. J., Heterogeneous chemistry on polar stratospheric clouds, *Atmos. Environ.*, *25*, 2535-2537, 1991.

Niedziela, R. F., R. E. Miller, and D. R. Worsnop, Temperature and frequency dependent optical constants for nitric acid dihydrate from aerosol spectroscopy, *J. Phys. Chem.*, *102*, 6477-6484, 1998a.

Niedziela, R F, M. L. Norman, R. E. Miller, and D. R. Worsnop, Temperature and composition dependent infrared optical constants for sulfuric acid, *Geophys. Res. Lett*, *25*, 4477-4480, 1998b.

Niedziela, R. F., M. L. Norman, C. L. DeForest, R. E. Miller, and D. R. Worsnop, A temperature and composition dependent study of H₂SO₄ optical constants using Fourier transform and tunable

diode laser infrared spectroscopy, *J. Phys. Chem.*, *103*, 8030-8040, 1999.

Palmer, K. F. and D. Williams, Optical constants of sulfuric acid: Application to the clouds of Venus?, *Appl. Opt.*, *14*, 208-219, 1975.

Palmer, K. F., B. E. Wood, and J. A. Roux, Infrared optical properties of solid mixtures of molecular species at 20 K, *AEDC-TR-80-30, AD-AO94214*, Arnold Eng. Dev. Cent., Air Force Syst. Command, Tennessee, 1981.

Querry, M. R., and I. L. Tyler, Reflectance and complex refractive indices in the infrared for aqueous solutions of nitric acid, *J. Chem. Phys.*, *72*, 2495-2499, 1980.

Remsberg, E. E., D. Lavery, and J. Crawford, Optical constants for sulfuric and nitric acids, *J. Chem. Eng. Data*, *19*, 263-265, 1974.

Richwine, L. J., M. L. Clapp, R. E. Miller, and D. R. Worsnop, Complex refractive indices in the infrared of nitric acid trihydrate aerosols, *Geophys. Res. Lett.*, *22*, 2625-2628, 1995.

Ritzhaupt, G., and J. P. Devlin, Ionic vs. molecular nature of monomeric ammonium and hydronium nitrate: Infrared spectra of $H_3O^+NO_3^-$ and $NH_4^+NO_3^-$ solvated in argon matrices, *J. Phys. Chem.*, *81*, 521-525, 1977.

Ritzhaupt, G., and J. P. Devlin, Infrared spectra of nitric and hydrochloric acid hydrate thin films, *J. Phys. Chem.*, *95*, 90-95, 1991.

Rothman, L. S., et al., The Hitran molecular database: Editions of 1991 and 1992, *J. Quant. Spectrosc. Radiat. Transfer*, *48*, 469-507, 1992.

Toon, O. B., and R. P. Turco, Polar stratospheric clouds and ozone depletion, *Sci. Am.*, *264* (6), 68-74, 1991.

Toon, O. B., M. A. Tolbert, B. G. Koehler, A. M. Middlebrook, and J. Jordan, The infrared optical constants of H₂O-ice, amorphous nitric acid solutions, and nitric acid hydrates, *J. Geophys. Res.*, *99*, 25,631-25,654, 1994.

Ulevicius, V., K. Willeke, S. A. Grinshpun, J. Donnelly, X. Lin, and G. Mainelis, Aerosolization of particles from a bubbling liquid: Characteristics and generator development, *Aerosol Sci. Technol.*, *26*, 175-190, 1997.

Waibel, A. E., T. Peter, K. S. Carslaw, H. Oelhaf, G. Wetzel, P. J. Crutzen, U. Poschl, A. Tsias, E. Reimer, and H. Fischer, Arctic ozone loss due to denitrification, *Science*, *283*, 2064-2069, 1999.

Worsnop, D. R., L. E. Fox, M. S. Zahniser, and S. C. Wofsy, Vapor pressures of solid hydrates of nitric acid: Implications for polar stratospheric clouds, *Science*, *259*, 71-74, 1993.

Young, T. F., L. F. Maranville, and H. M. Smith, Raman spectral investigations of ionic equilibria in solutions of strong electrolytes. in *The Structure of Electrolytic Solutions*, edited by W. J. Hamer, vol. 1, pp. 35-63, John Wiley, New York, 1959.

M. L. Norman, R. E. Miller, and J. Qian, Department of Chemistry, University of North Carolina, CB 3290 Venable Hall, Chapel Hill, NC 27599-3290. (remiller@unc.edu)

D. R. Worsnop, Center for Aerosol and Cloud Chemistry, Aerodyne Research, Inc., Billerica, MA 01821-3976.